INTERNATIONAL JOURNAL FOR NUMERICAL METHODS IN FLUIDS
Int. J. Numer. Meth. Fluids 2007; **55**:1189–1211
Published online 6 June 2007 in Wiley InterScience (www.interscience.wiley.com). DOI: 10.1002/fld.1522

An improved hybrid Cartesian/immersed boundary method for fluid–solid flows

Tong Gao[1], Yu-Heng Tseng[2] and Xi-Yun Lu[1,*,†]

[1]*Department of Modern Mechanics, University of Science and Technology of China, Anhui, Hefei 230026, China*
[2]*Department of Atmospheric Sciences, National Taiwan University, Taipei, Taiwan*

SUMMARY

An improved hybrid Cartesian/immersed boundary method is proposed based on ghost point treatment. A second-order Taylor series expansion is used to evaluate the values at the ghost points, and an inverse distance weighting method to interpolate the values due to its properties of preserving local extrema and smooth reconstruction. The present method effectively eliminates numerical instabilities caused by matrix inversion and flexibly adopts the interpolation in the vicinity of the boundary. Some typical fluid–solid flows, including viscous flow past a circular cylinder, a sphere, two cylinders in a side-by-side arrangement, and an array of 18 staggered cylinders, are examined. These benchmark simulations reasonably indicate the reliability and capability of the present method. Copyright © 2007 John Wiley & Sons, Ltd.

Received 21 August 2006; Revised 3 April 2007; Accepted 4 April 2007

KEY WORDS: immersed boundary method; Taylor series expansion; inverse distance weighting; fluid–solid interaction

1. INTRODUCTION

Numerical simulation of flow over a rigid or flexible body with complex immersed boundary is a challenging problem in computational fluid dynamics. In the last decades, extensive attentions have been paid to the development of efficient numerical methods to study the flow in complex geometry and fluid–structure interaction. Usually, boundary-fitted curvilinears or unstructured grids are employed to deal with such a problem [1–3]. However, there are some difficulties to limit the application of the numerical methods. High storage requirements are needed on the grid generation

*Correspondence to: Xi-Yun Lu, Department of Modern Mechanics, University of Science and Technology of China, Anhui, Hefei 230026, China.
†E-mail: xlu@ustc.edu.cn

Contract/grant sponsor: National Natural Science Foundation of China; contract/grant numbers: 90405007, 10332040
Contract/grant sponsor: National Science Council; contract/grant number: 95-2119-M-002-048

for complex geometry. The computation is even more expensive and time consuming for moving boundary problem because the mesh must be regenerated each time step to adapt the moving boundary. In addition, large deformation of the boundary is hardly achievable since high quality of the boundary-fitted mesh is not guaranteed.

To overcome these difficulties, some efficient non-boundary conforming methods, e.g. immersed boundary method (IBM), have been proposed. The IBM has the advantage of easily treating complex fluid–structure interaction problems since the governing equations are solved on a fixed Cartesian grid. The boundary conditions are implemented by evaluating the values at the grid nodes just in the vicinity of the immersed boundary. In the IBM, an external force field $\mathbf{f}$ is generated and added to the Navier–Stokes (N–S) equations to mimic the boundary immersed in the fluid flow, i.e.

$$\frac{\partial \mathbf{u}}{\partial t} + \mathbf{u} \cdot \nabla \mathbf{u} = -\frac{1}{\rho} \nabla p + \nu \nabla^2 \mathbf{u} + \mathbf{f} \tag{1}$$

$$\nabla \cdot \mathbf{u} = 0 \tag{2}$$

where $\mathbf{u}$ is the velocity vector, ρ the density, p the pressure, and ν the kinematic viscosity of the fluid, respectively. The IBM originates from Peskin's work for two-dimensional (2D) blood flows at low Reynolds numbers [4, 5] and has been applied to various biological fluid–structure interaction problems [6, 7]. In Peskin's IBM, a discrete Dirac δ function is introduced to spread the boundary forcing term over a few grid nodes near the boundary where the sharp interface is smeared to the thickness about the order of mesh width [8]. Then, Goldstein *et al.* [9] developed a virtual boundary method to deal with stationary solid boundary *via* a feedback forcing approach. However, the discrete Dirac δ function smears the boundary surface leading to only first-order accuracy on the boundary. Large artificial stiffness is needed to implement the no-slip boundary condition for flow past a rigid body and greatly affects the stability of the algorithm.

Recently, some IBMs have been developed and applied to a variety of problems. A cut-cell method, which tracks the immersed boundary as a sharp interface and reshapes the boundary cells to fit the local geometry, was proposed [10, 11]. The computational stencils are directly modified in the immediate vicinity of the immersed boundary using a quadratic interpolation. However, this method encounters a difficulty that the intersections of immersed interface and Cartesian grids may have complex topology. Then, LeVeque and Li [12] proposed an immersed interface method (IIM) in which the external forcing field is constructed by incorporating accurate jump conditions across the interface. This method was first applied to elliptic and Stokes equations, and then extended to the 2D N–S equations [13]. The IIM overcomes the limitation of discrete Dirac δ function in Peskin's IBM and can achieve second or even higher-order accuracy. Xu and Wang [14, 15] extended the IIM to the three-dimensional (3D) problems by systematically deriving the jump conditions of all spatial and temporal derivatives of the velocity and pressure for the 3D N–S equations.

Fadlun *et al.* [16] developed a new variant of the IBM based on the idea of 'direct forcing' [17]. This method is called the hybrid Cartesian/immersed boundary (HCIB) approach [18]. The solid boundary is treated as a sharp interface and the desired velocities are imposed on the grid nodes close to the boundary surface, referred to as 'forcing points'. By adding the forcing term to the N–S equation, the semi-discrete form is represented as

$$\frac{\mathbf{u}^{n+1} - \mathbf{u}^n}{\Delta t} = \mathbf{RHS}^{n+1/2} + \mathbf{f}^{n+1/2} \tag{3}$$

DOI: 10.1002/fld

where $\mathbf{RHS}^{n+1/2}$ contains the convective, viscous, and pressure gradient terms. By directly imposing velocity condition $\mathbf{u}^{n+1} = \mathbf{V}^{n+1}$ on the immersed boundary, the forcing term can be easily evaluated as

$$\mathbf{f}^{n+1/2} = -\mathbf{RHS}^{n+1/2} + \frac{\mathbf{V}^{n+1} - \mathbf{u}^{n}}{\Delta t} \tag{4}$$

Similar to the cut-cell method, local stencil is used to reconstruct the $\mathbf{f}^{n+1/2}$ combining with the boundary conditions. It avoids the dynamic process (such as artificial stiffness) introduced in Peskin's IBM or explicit derivations of jump conditions in IIM. Less computation is required in the solver since no new term is involved, and the stability of time advancement scheme is not affected. The HCIB approach with direct forcing is attractive in dealing with complex geometry due to its simplicity in the boundary treatment, and therefore has been applied to various problems [16–22]. However, the boundary treatment by polynomials in the HCIB approach may cause numerical instabilities since the matrix inversions must be solved expensively and are easily ill-conditioned or singular [19]. Thus, the relevant improvements on the HCIB method are still desirable.

In the present study, we propose an improved HCIB method based on ghost point treatment. In this method, the forcing points inside the body or the ghost points are adopted to impose the boundary conditions on the immersed boundary surface. Then, a second-order Taylor series expansion rather than polynomials is used to obtain the values at the ghost points so that the matrix inversions are avoided. An inverse distance weighting (IDW) interpolation is employed to select stencil nodes flexibly in the vicinity of the boundary leading to accelerating the convergence. Further, the present method is validated using some typical fluid–solid flows.

This paper is organized as follows. The present method is described in Section 2. Then, in Section 3, the method is applied to some typical 2D and 3D flows, including viscous flow past a cylinder, a sphere, two cylinders in a side-by-side arrangement, and an array of 18 staggered cylinders. Finally, concluding remarks are given in Section 4.

2. METHODOLOGY

2.1. Obtaining the values at the forcing points

How to specify the values at the forcing points in the vicinity of the immersed boundary for accurately satisfying boundary conditions is a critical issue in the HCIB method. Here, we use the forcing points inside the boundary, i.e. ghost points, similar to the treatment by Tseng and Ferziger [19]. To present the boundary treatment, a typical schematic of the ghost point arrangement is shown in Figure 1, where two nearest fluid nodes X_1, X_2 and a boundary node O are used to linearly extrapolate the value at the ghost point G. The boundary node O can be chosen as the mid-point of the boundary segment within the cell or the point on the boundary at which **GO** is normal to the boundary. However, some numerical difficulties occur in the calculations [19–23]. When the boundary is close to a fluid node, the inversions for different matrices may tend to be ill-conditioned and even become more serious for higher-order reconstruction polynomials. When the boundary node is close to one of the fluid nodes used in the extrapolation, the absolute value at the ghost point G may be much greater than the values of the nearby fluid nodes X_i, leading to numerical divergence.

DOI: 10.1002/fld

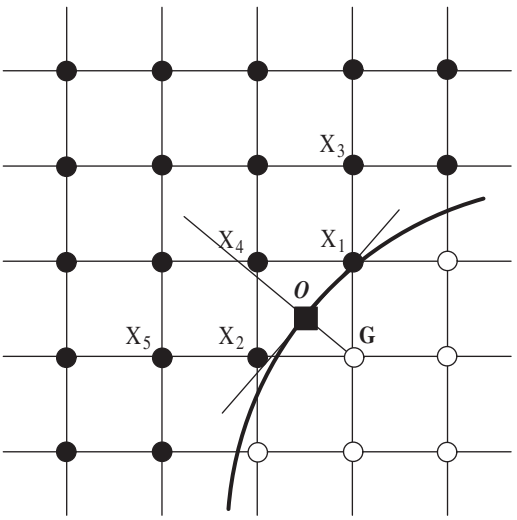

Figure 1. Schematic of the points used to evaluate the variable at a ghost point G.

To overcome these difficulties, we thus propose an improved HCIB method using Taylor series expansion to reconstruct the value at the ghost point. For neatness, we mainly discuss 2D case here and can easily extend to 3D case. As shown in Figure 1, the value at the ghost point G can be expressed as

$$\phi_G = \phi_O + \sum_{k=1}^{s} \frac{1}{k!} \left(\Delta x \frac{\partial}{\partial x} + \Delta y \frac{\partial}{\partial y} \right)^k \phi_O + R_s \tag{5}$$

where $\Delta x = x_G - x_O$, $\Delta y = y_G - y_O$, and R_s is the remainder term of the Taylor series of degree s, defined as

$$R_s = \frac{1}{(s+1)!} \left(\Delta x \frac{\partial}{\partial x} + \Delta y \frac{\partial}{\partial y} \right)^{s+1} \phi_O \sim O(\Delta x^{s+1}, \Delta y^{s+1}) \tag{6}$$

The operator $(\Delta x(\partial/\partial x) + \Delta y(\partial/\partial y))$ acts on the boundary node yielding the kth-order derivative,

$$\left(\Delta x \frac{\partial}{\partial x} + \Delta y \frac{\partial}{\partial y} \right)^k \phi_O = \sum_{i=0}^{k} C_k^i \Delta x^i \Delta y^{k-i} \frac{\partial^k \phi_O}{\partial x^i \partial y^{k-i}} \tag{7}$$

where C_k^i is the coefficient of binomial, i.e.

$$C_k^i = \frac{k!}{i!(k-i)!}$$

Generally, as indicated by Ferziger and Perić [24], a second-order approximation is able to offer a reasonable combination of accuracy, ease of use, and cost-effectiveness in numerical calculations. Thus, a second-order Taylor expansion is used to evaluate the value of point G, and its formulation

DOI: 10.1002/fld

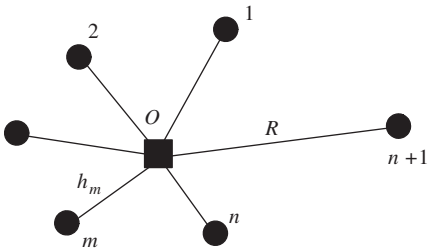

Figure 2. Schematic of the points used in the IDW interpolation.

with respect to node O is represented as

$$\phi_G = \phi_O + \frac{\partial \phi_O}{\partial x}\Delta x + \frac{\partial \phi_O}{\partial y}\Delta y + \frac{1}{2}\left(\frac{\partial^2 \phi_O}{\partial x^2}\Delta x^2 + 2\frac{\partial^2 \phi_O}{\partial x \partial y}\Delta x \Delta y + \frac{\partial^2 \phi_O}{\partial y^2}\Delta y^2\right) + O(\Delta x^3, \Delta y^3) \tag{8}$$

Since the value of node O is known from accurate Dirichlet boundary conditions, the value ϕ_G can be solved when the first- and second-order derivatives at the node O in Equation (8) are obtained below.

2.2. Reconstruction of the derivatives

To reliably reconstruct the derivatives, the nodes for reconstruction are usually selected around the boundary node O. Here we use the IDW interpolation to evaluate derivatives. The IDW is a weight-averaged method proposed by Franke [25] and holds the properties of preserving local maxima and producing smooth reconstruction. As shown in Figure 2, the formulation of the IDW can be expressed as

$$\phi_O = \frac{1}{q}\sum_{m=1}^{n} w_m \phi_m \tag{9}$$

$$w_m = \left(\frac{R - h_m}{R h_m}\right)^p \tag{10}$$

$$q = \sum_{l=1}^{n}\left(\frac{R - h_l}{R h_l}\right)^p \tag{11}$$

where ϕ_O represents the value at an interpolated point O, ϕ_m and w_m are the value and weighting coefficient, respectively, h_m is the distance between O and mth stencil node, p is a positive real number called the power parameter (typically $p = 2$), R denotes the distance from O to the most distant stencil node used for interpolation, and n is the total number of the stencil nodes. The power parameter p in Equation (10) ensures the weighting coefficient w_m to drop off smoothly when the distance from point O increases. Note that, when n nodes are used to interpolate, there are actually $n + 1$ nodes selected in the reconstruction stencil. The additional one is only used to define the largest distance R without contribution to the interpolated value.

DOI: 10.1002/fld

Further, as indicated by Watson and Philip [26], the derivatives at the point O can be calculated using the IDW, e.g. the first and second derivatives,

$$\frac{\partial \phi_O}{\partial x} = \frac{1}{q} \sum_{m=1}^{n} w_m \frac{\partial \phi_m}{\partial x} \tag{12}$$

$$\frac{\partial \phi_O}{\partial y} = \frac{1}{q} \sum_{m=1}^{n} w_m \frac{\partial \phi_m}{\partial y} \tag{13}$$

$$\frac{\partial^2 \phi_O}{\partial x^2} = \frac{1}{q} \sum_{m=1}^{n} w_m \frac{\partial^2 \phi_m}{\partial x^2} \tag{14}$$

$$\frac{\partial^2 \phi_O}{\partial y^2} = \frac{1}{q} \sum_{m=1}^{n} w_m \frac{\partial^2 \phi_m}{\partial y^2} \tag{15}$$

$$\frac{\partial^2 \phi_O}{\partial x \partial y} = \frac{1}{q} \sum_{m=1}^{n} w_m \frac{\partial^2 \phi_m}{\partial x \partial y} \tag{16}$$

All the derivatives on the right-hand side of Equations (12)–(16) are calculated by the central finite difference approximations with the values at previous time step, e.g. the first- and second-order derivatives in the x-direction,

$$\frac{\partial \phi_i}{\partial x} = \frac{\phi_{i+1} - \phi_{i-1}}{2\Delta x} \tag{17}$$

$$\frac{\partial^2 \phi_i}{\partial x^2} = \frac{\phi_{i+1} - 2\phi_i + \phi_{i-1}}{\Delta x^2} \tag{18}$$

Based on our extensive tests, it is enough to keep the calculation accuracy to employ usually 3–4 stencil nodes in 2D case or 4–5 nodes in 3D case which are most close to point O in the reconstruction of the derivatives.

2.3. The full expression of value at the ghost point

Substituting Equations (9) and (12)–(16) into Equation (8), we can construct the new HCIB method based on the ghost point treatment using the Taylor series expansion and IDW interpolation described above. The value at the ghost point is obtained by

$$\begin{aligned} \phi_G = {} & \frac{1}{q} \sum_{m=1}^{n} w_m \phi_m + \frac{1}{q} \left(\sum_{m=1}^{n} w_m \frac{\partial \phi_m}{\partial x} \Delta x + \sum_{m=1}^{n} w_m \frac{\partial \phi_m}{\partial y} \Delta y \right) \\ & + \frac{1}{2q} \left(\sum_{m=1}^{n} w_m \frac{\partial^2 \phi_m}{\partial x^2} \Delta x^2 + 2 \sum_{m=1}^{n} w_m \frac{\partial^2 \phi_m}{\partial x \partial y} \Delta x \Delta y + \sum_{m=1}^{n} w_m \frac{\partial^2 \phi_m}{\partial y^2} \Delta y^2 \right) \\ & + O(\Delta x^3, \Delta y^3) \end{aligned} \tag{19}$$

DOI: 10.1002/fld

Furthermore, Dirichlet boundary condition of the velocity ($\mathbf{u} = \mathbf{V}|_{\partial b}$) can be specified by replacing the first term in Equation (19):

$$\frac{1}{q}\sum_{m=1}^{n} w_m \phi_m = \phi|_{\partial b} \tag{20}$$

Then, the value at the ghost point is evaluated as

$$\begin{aligned}\phi_G = \phi|_{\partial b} &+ \frac{1}{q}\left(\sum_{m=1}^{n} w_m \frac{\partial \phi_m}{\partial x}\Delta x + \sum_{m=1}^{n} w_m \frac{\partial \phi_m}{\partial y}\Delta y\right) \\ &+ \frac{1}{2q}\left(\sum_{m=1}^{n} w_m \frac{\partial^2 \phi_m}{\partial x^2}\Delta x^2 + 2\sum_{m=1}^{n} w_m \frac{\partial^2 \phi_m}{\partial x \partial y}\Delta x \Delta y + \sum_{m=1}^{n} w_m \frac{\partial^2 \phi_m}{\partial y^2}\Delta y^2\right) \\ &+ O(\Delta x^3, \Delta y^3)\end{aligned} \tag{21}$$

The corresponding 3D formulation can be straightly obtained from the above procedure. It is needed to indicate that, when the boundary happens to overlap certain grid nodes, such as moving boundary or complex geometry of the immersed body, singularities may occur in Equation (10). In this situation, we may simply reset the weighting coefficient of the nearest stencil node to be 1 and others 0. This treatment equivalently moves the boundary node O to the nearest stencil node. Compared with the approach proposed by Tseng and Ferziger [19], the present method can effectively remove the relevant numerical instabilities.

2.4. The basic solver of the algorithm

A fractional-step method is employed to solve the N–S equations (1) and (2) based on an improved projection method [27–29]. The velocity field is corrected by the pressure to satisfy the continuity equation. The convective and viscous terms are approximated using Adams–Bashforth and Crank–Nicholson schemes, respectively. All spatial derivatives are discretized using the second-order central difference scheme in a staggered grid [30]. Since the velocity and pressure are defined at different grid locations, as shown in Figure 3, the ghost points are also used in the staggered grid. Here, the semi-discrete form can be obtained by splitting Equation (1) into four substeps:

$$\frac{\hat{\mathbf{u}} - \mathbf{u}^n}{\Delta t} = \frac{1}{2}(3\mathbf{H}(\mathbf{u}^n) - \mathbf{H}(\mathbf{u}^{n-1})) - \mathbf{G}p^n + \frac{1}{2Re}(\mathbf{L}(\hat{\mathbf{u}}) + \mathbf{L}(\mathbf{u}^n)) + \mathbf{f}^{n+1/2} \tag{22}$$

$$\mathbf{L}(\phi^{n+1}) = \frac{1}{\Delta t}\mathbf{D}(\hat{\mathbf{u}}) \tag{23}$$

$$\mathbf{u}^{n+1} = \hat{\mathbf{u}} - \Delta t \mathbf{G}(\phi^{n+1}) \tag{24}$$

$$p^{n+1} = p^n + \phi^{n+1} - \frac{\Delta t}{2Re}\mathbf{L}(\phi^{n+1}) \tag{25}$$

where **H**, **G**, **L** and **D** represent the discrete convection, gradient, Laplace and divergence operator, respectively, and are described as

$$\mathbf{H} = -u\frac{\delta}{\delta x_1} - v\frac{\delta}{\delta x_2} - w\frac{\delta}{\delta x_3}, \quad \mathbf{G} = \frac{\delta}{\delta x_i}, \quad \mathbf{L} = \frac{\delta^2}{\delta x_1^2} + \frac{\delta^2}{\delta x_2^2} + \frac{\delta^2}{\delta x_3^2}$$

DOI: 10.1002/fld

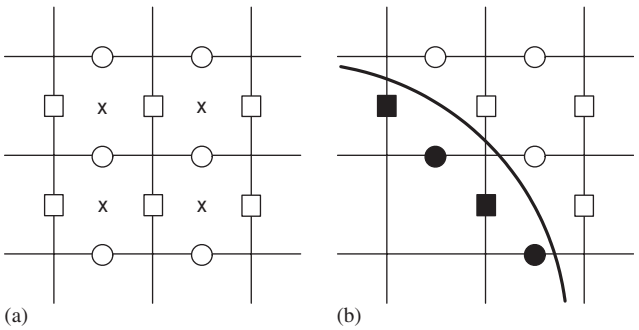

Figure 3. (a) Locations of fluid variables, where □ denotes the location of U component, ○ the location of V component, × the location of p component and (b) staggered arrangement of the ghost points, where ■ denotes the location of U component, • the location of V component.

$$\mathbf{D} = \frac{\delta}{\delta x_1} + \frac{\delta}{\delta x_2} + \frac{\delta}{\delta x_3}$$

To set the boundary condition of the velocity, i.e. $\mathbf{u} = \mathbf{V}|_{\partial b}$, we have

$$\mathbf{f}^{n+1/2} = -\mathbf{RHS}^{n+1/2} + \frac{\mathbf{V}|_{\partial b}^{n+1} - \mathbf{u}^n}{\Delta t} \tag{26}$$

The forcing term $\mathbf{f}^{n+1/2}$ requires the unknowns on the grid coincide with the immersed boundary, which may be inaccessible for the immersed bodies with complex curvilinear geometries. Usually, there are mainly two groups of forcing treatments [19, 31, 32]. One is spreading the forcing function over the vicinity of the immersed boundary surface [4–9], and the other producing a local reconstruction of the solution on the boundary values [18–22, 33]. Our treatment belongs to the second category. As indicated above, the boundary conditions $\mathbf{u} = \mathbf{V}|_{\partial b}$ can be reliably imposed using Equation (21).

The Poisson equation (23) is solved by the biconjugate gradient stabilized (Bi-CGSTAB) iteration method, which belongs to Krylov subspace methods [34, 35] with very efficient performance to treat sparse matrices. To accelerate the convergence of the solver and maintain the stability of the calculation, Stone's strongly implicit procedure [36] is also used as the preconditioner of the Bi-CGSTAB iteration.

We now summarize the full solution procedure of the present method:

(1) Detect the ghost point G and boundary node O, and select fluid nodes X_i. Then determine the weighting coefficient of each stencil node with the IDW to evaluate the desired derivatives at the boundary node O.
(2) Impose boundary conditions implicitly through the ghost point G by the second-order Taylor series expansion in Equation (21), and update the values at the ghost point by the Adams–Bashforth scheme to maintain the second-order accuracy in time.
(3) Solve Equation (22) to obtain the intermediate velocity $\hat{\mathbf{u}}$.

DOI: 10.1002/fld

(4) Compute the pressure correction by solving Equation (23).
(5) Update the velocity $\mathbf{u}^{n+1}$ in Equation (24) and pressure p^{n+1} in Equation (25) by Equation (23).

3. NUMERICAL RESULTS

To validate the accuracy of the present method, some typical flows, including viscous flow past a circular cylinder, a sphere and multiple cylinders, are numerically simulated, and the calculated results are discussed.

3.1. Uniform flow past a circular cylinder

Uniform flow past a circular cylinder is simulated in a rectangular domain $l \times h = 45D \times 30D$, where D is the cylinder diameter. The computational domain and the boundary conditions at far boundaries are shown in Figure 4. The same kind of the boundary conditions at far boundaries is also used in the following cases. The Reynolds number is defined as $Re = UD/v$, where U is the free-stream velocity, and v the kinematic viscosity. When Re is less than about 47, the flow is steady with two symmetrical recirculating vortices behind the cylinder. When Re increases, vortex shedding from the cylinder occurs. Here, some typical results for $Re = 20$ up to 160 are presented.

In the present calculation, we use three stencil nodes (i.e. total four nodes) to interpolate the value at the ghost point. A grid resolution study is first performed to investigate the influence of mesh widths (i.e. $0.015D$, $0.03D$ and $0.06D$) on the result. A time step is chosen as $\Delta t = 10^{-3}$ in this case and the following cases, which has been validated to be reliable on the calculated results.

Figure 5 shows the streamlines with two symmetrical recirculating zones behind the cylinder at $Re = 40$. Then, Table I exhibits the recirculation length l_w and the drag coefficient C_D, where l_w is the distance between two stagnation points indicated in Figure 5. Compared with these data calculated by different mesh widths, the results can be predicted reliably when the mesh width is $0.03D$. In all the cases shown later, we will use the mesh width $0.03D$ for the calculations. Further, Figure 6 shows the distributions of the pressure coefficient (C_p) and skin-friction coefficient (C_f) along the cylinder surface obtained by linear extrapolation with nearest fluid nodes outside.

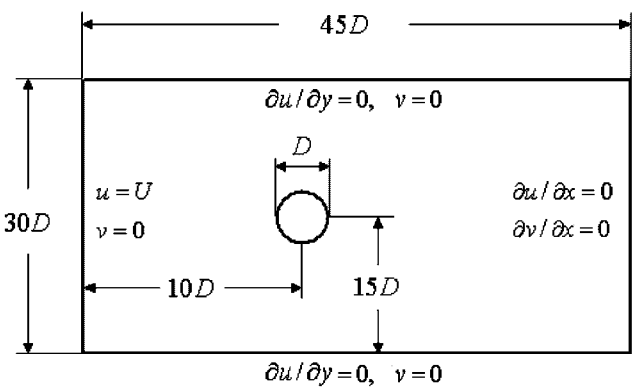

Figure 4. The computational domain and external boundary conditions for flow past a circular cylinder.

DOI: 10.1002/fld

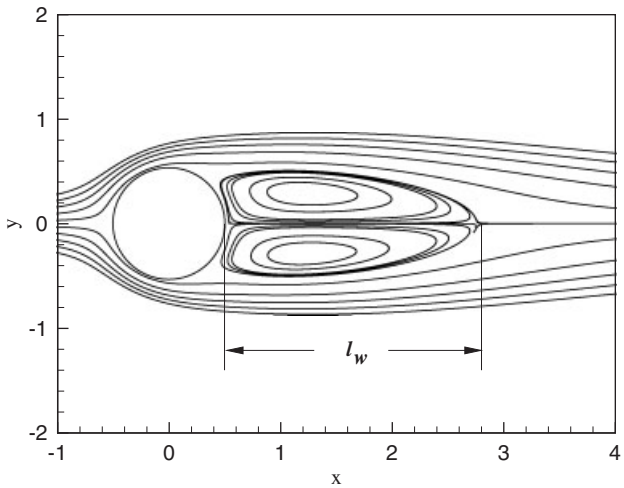

Figure 5. Streamlines of flow around a cylinder at $Re = 40$.

Table I. The recirculation zone length l_w and drag coefficient C_D at $Re = 40$.

	l_w/D	C_D
Present study		
(Mesh width $= 0.06D$)	2.23	1.57
(Mesh width $= 0.03D$)	2.24	1.58
(Mesh width $= 0.015D$)	2.24	1.58
Tseng and Ferziger [19]	2.21	1.53
Ye *et al.* [10]	2.27	1.58

To deal with the grid sensitivity, we perform an additional simulation with a finest mesh (i.e. mesh width $0.005D$) and use this result to act as an exact solution. Meanwhile, the calculations using linear and quadratic GCIBM treatments are also performed on the same mesh widths. Here, L_∞ and L_2 norms of error are calculated by

$$\varepsilon_\infty = \max_{i=1,N} |u_i - u_i^e|, \quad \varepsilon_2 = \left[\frac{1}{N} \sum_{i=1}^{N} |u_i - u_i^e|^2 \right]^{1/2} \tag{27}$$

where N is the total number of the grid nodes used, and u_i^e represents the solution at the finest mesh. As shown in Figures 7 and 8, the grid convergence of U and V components predicted by the present method exhibits that both the L_∞ and L_2 norms of error are consistent to second-order accuracy, indicating that the method can achieve the second-order accuracy. Comparing with the previous quadratic GCIBM [19], the present method is without reducing accuracy.

The convergence rates of the steady-state solution calculated by the present method and previous GCIBM [19] are given in Figure 9. It is seen that the present HCIB method converges rapidly and smoothly. Since the positive power parameter p of IDW interpolation can effectively smooth out the initial errors, the present method maintains a good convergence and stability performance.

DOI: 10.1002/fld

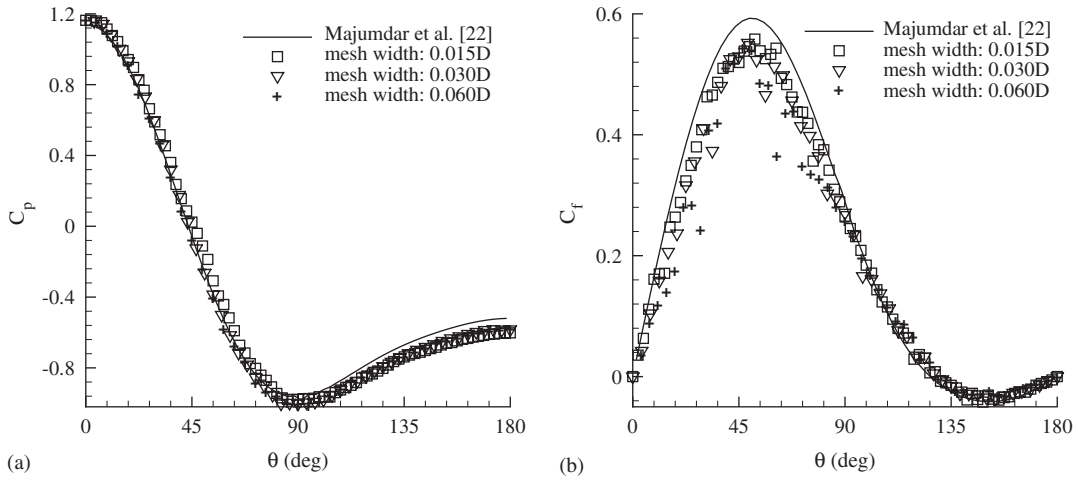

Figure 6. Distributions of (a) the pressure coefficient C_p and (b) skin-friction coefficient C_f.

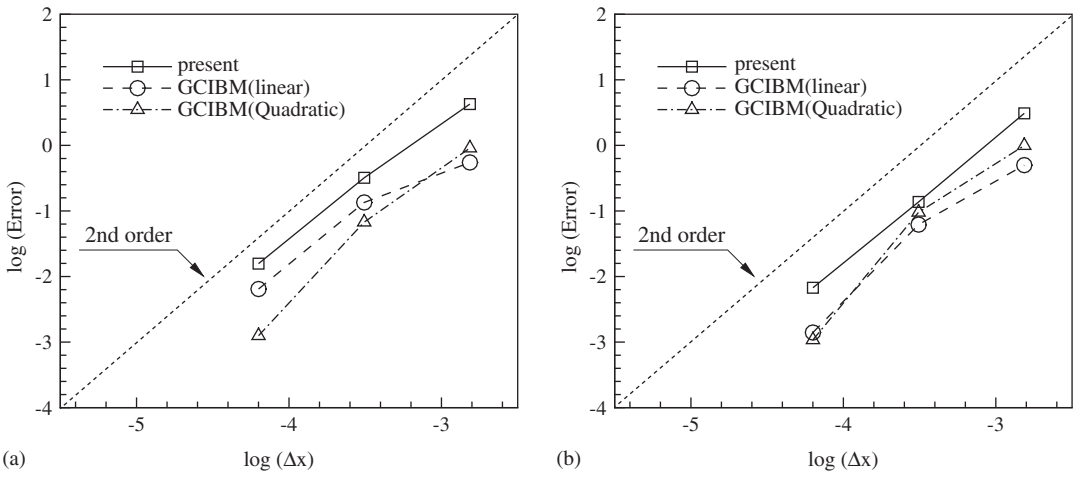

Figure 7. L_∞ norm error of velocity: (a) U component and (b) V component.

To demonstrate the force behaviour, the drag and lift coefficients are defined as $C_{\mathrm{D}} = F_x/(\frac{1}{2}\rho U^2 D)$ and $C_{\mathrm{L}} = F_y/(\frac{1}{2}\rho U^2 D)$, respectively, where F_x and F_y are the drag and lift force acting on the cylinder, respectively. The mean drag coefficient predicted by the present method are given in Table II and agree well with the previous results. Figure 10 shows the lift coefficient fluctuation C'_{L} (i.e. maximum deviation from the time-averaged value) and Strouhal number St, which are also in good agreement with the data obtained by the boundary-fitted simulations.

Instantaneous vorticity contours are shown in Figure 11. Steady separation bubbles are formed at $Re = 40$ behind the cylinder and alternative vortex shedding from the cylinder occurs at

DOI: 10.1002/fld

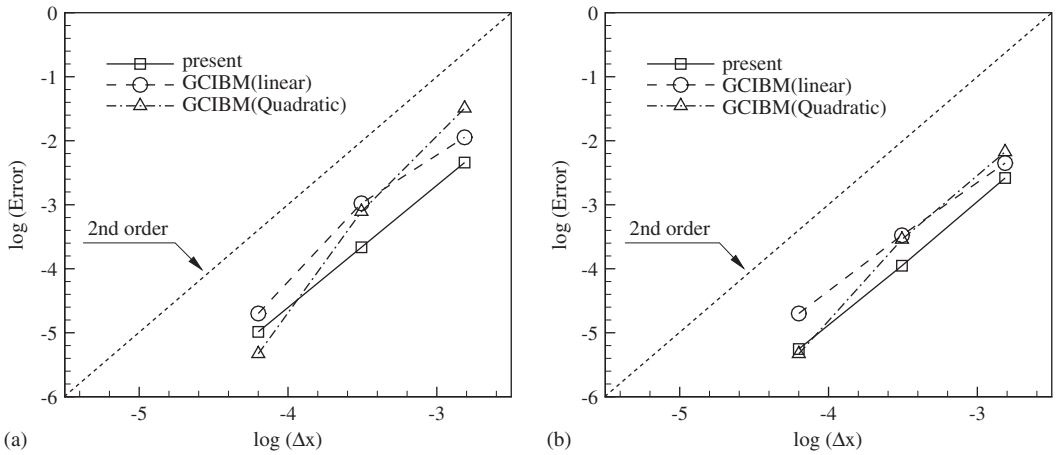

Figure 8. L_2 norm error of velocity: (a) U component and (b) V component.

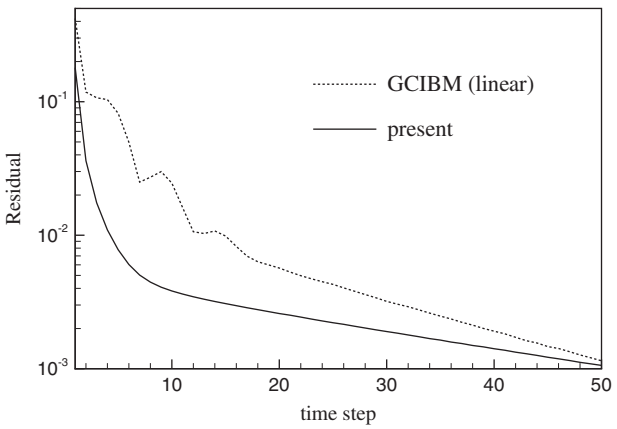

Figure 9. The convergence rates of GCIBM with linear extrapolation and present method.

Table II. Comparison of the mean drag coefficient $\bar{C}_D$ with previous data.

Re	Present results	Park *et al.* [37]	Lima e Silva *et al.* [38]	Ye *et al.* [10]	Tritton [39]	Tseng and Ferziger [19]
20	2.09	2.01	2.04	2.03	2.22	—
40	1.58	1.51	1.54	1.52	1.48	1.53
60	1.44	1.39	—	—	—	—
80	1.40	1.35	1.40	1.37	1.29	—
100	1.39	1.33	1.39	—	—	1.42
120	1.38	1.32	—	—	—	—
140	1.38	1.32	—	—	—	—
160	1.38	1.32	—	—	—	—

DOI: 10.1002/fld

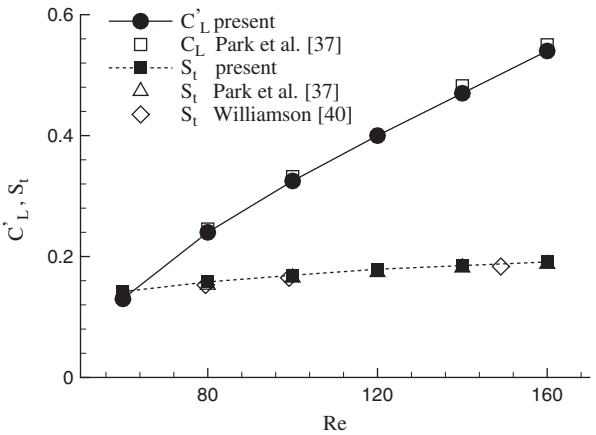

Figure 10. Lift coefficient fluctuation (C'_{L}) and Strouhal number (St) *versus* the Reynolds number.

$Re = 60$ and 100. Meanwhile, the corresponding drag and lift coefficients are reasonably calculated and shown in Figure 12 for $Re = 40$ and 100.

We have also performed some tests for the flow past an oscillating circular cylinder using the present method coupled with an approach proposed by Kim and Choi [41]. In the moving boundary case, since the velocity and pressure unknowns are only located outside the immersed body, the positions of these unknowns are different from time to time. To avoid the difficulty in the treatment of the change of these positions, an IBM using a non-inertial reference frame fixed to the moving rigid body [41] is applied to the present simulation. Based on our extensive tests, e.g. the flow past a transversely oscillating circular cylinder (not shown here), the present method can reliably deal with the moving boundary flows.

3.2. Uniform flow past a 3D sphere

Uniform viscous flow past a 3D stationary sphere is investigated. The Reynolds number is defined as $Re = UD/v$ based on the free stream velocity U, the diameter of the sphere D, and the kinematic viscosity v. According to previous studies [42, 43], flow separation behind the sphere occurs when Re reaches 24. A vortex ring thereby attached to the sphere remains stable and axisymmetric up to $Re = 210$. When $210 < Re < 270$, the transitional regime from 2D axisymmetric to 3D unsteady flows is observed. The flow structure becomes non-axisymmetric and the vortex ring shifts off the plane perpendicular to the axis. When $Re > 270$, unsteady vortex shedding occurs to form complex 3D vortex structures.

The computational domain has the size of $l \times w \times h = 22D \times 12D \times 12D$ with both the mesh widths $0.03D$ and $0.06D$. In the 3D case, as shown in Figure 13, the reconstruction stencil of IDW interpolation uses four nodes for the present calculation.

Table III shows the mean drag coefficient and some previous data obtained by IBM [16] and boundary-fitted methods [43, 44], where the drag coefficient is defined as $C_{\mathrm{D}} = F_x/(\frac{1}{2}\rho U^2 \cdot \pi D^2/4)$. It is seen that our results for the mesh width $0.03D$ agree well with the previous data, even though the results for the coarse mesh width $0.06D$ are somewhat smaller.

DOI: 10.1002/fld

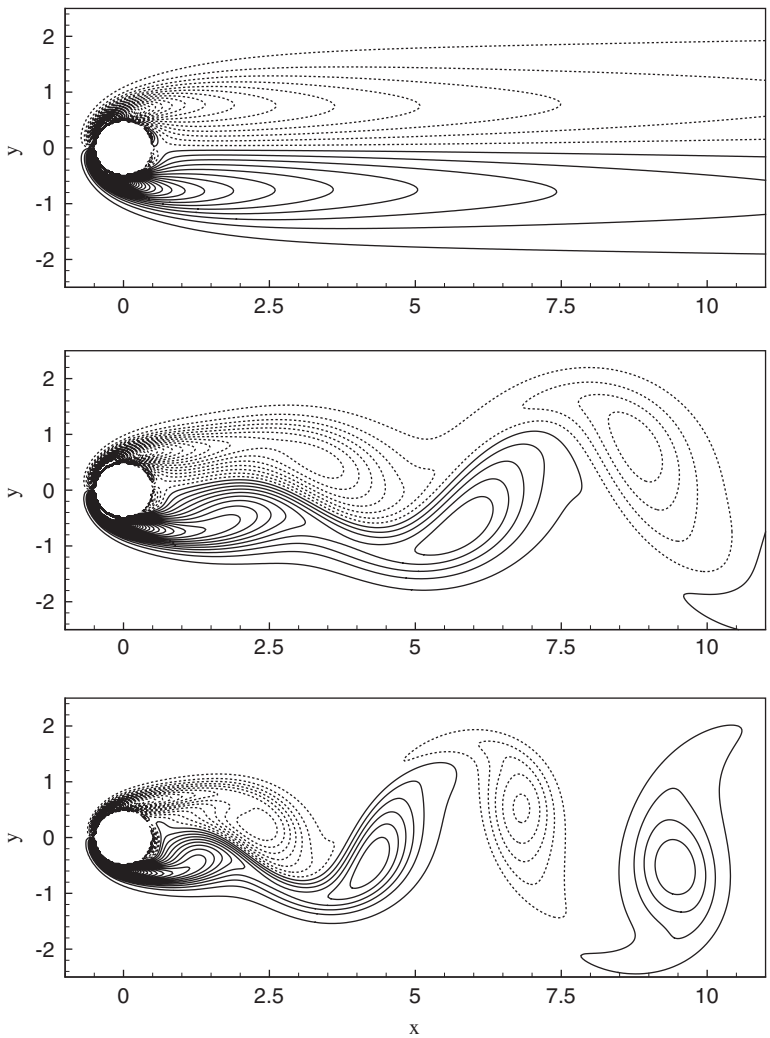

Figure 11. Instantaneous vorticity contours at $Re = 40$, 60 and 100 (from top to bottom).

To demonstrate the vortical structures, the vortex cores based on the definition by Jeong and Hussain [45] are shown in Figure 14 for $Re = 100$ and 300. The 3D vortex structure is axisymmetric at $Re = 100$. With the increase of Re, e.g. $Re = 300$, unsteady vortex shedding occurs.

3.3. Flow past multi-cylinder

The viscous flow past multi-cylinder is further investigated to analyse the flow structures and force behaviours. Here, we mainly consider two typical cases. One is a uniform flow past two cylinders in a side-by-side arrangement, and the other a flow past an array of 18 cylinders in a staggered arrangement.

DOI: 10.1002/fld

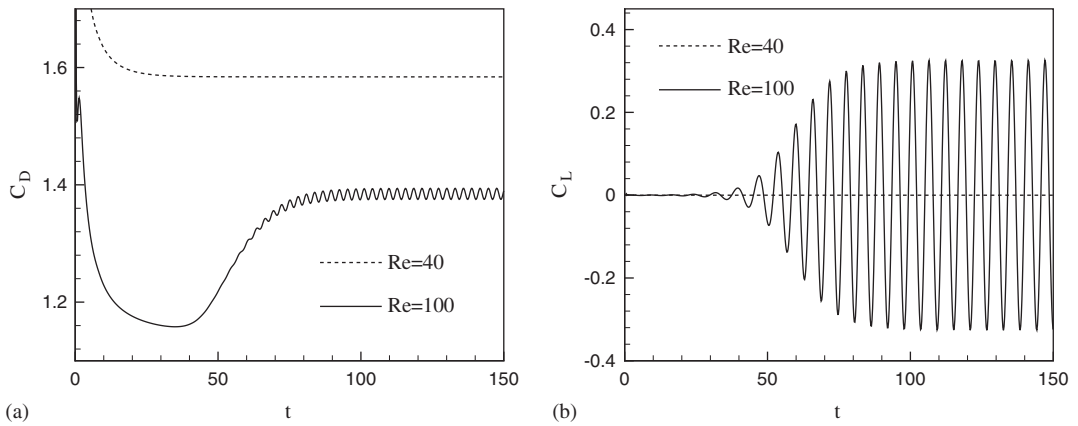

Figure 12. Evolution of force coefficients: (a) drag coefficient C_D and (b) lift coefficient C_L.

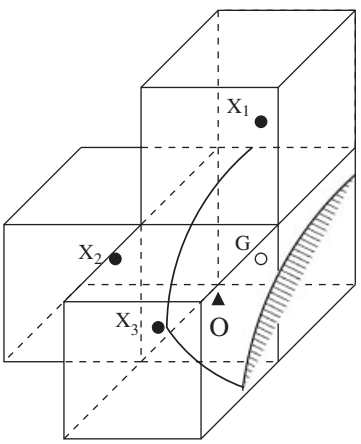

Figure 13. Schematic of the points used to evaluate the value at the ghost point in 3D case.

Table III. Comparison of the mean drag coefficient $\bar{C}_D$ with previous data.

	Re	$\bar{C}_D$
Present study (mesh width $= 0.06D$)	100	1.01
	300	0.60
Present study (mesh width $= 0.03D$)	100	1.09
	300	0.66
Fadlun *et al.* [16]	100	1.08
Johnson and Patel [43]	100	1.10
	300	0.66
Constantinescu and Squires [44]	300	0.66

DOI: 10.1002/fld

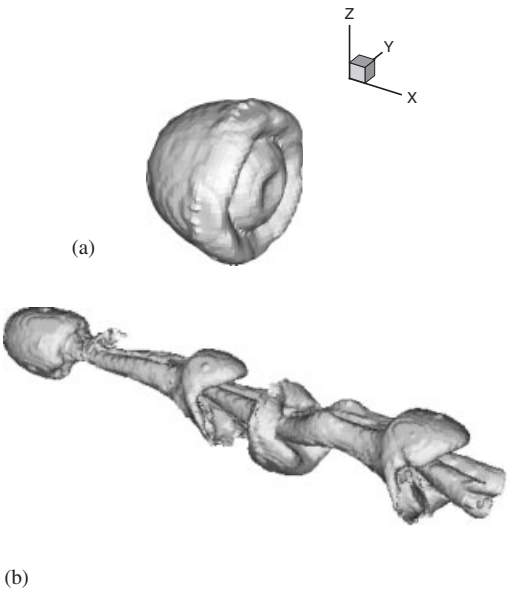

Figure 14. Instantaneous vortex cores of flow past a sphere: (a) $Re = 100$ and (b) $Re = 300$.

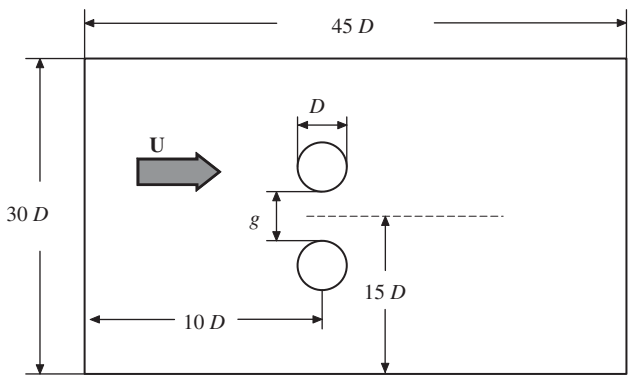

Figure 15. Schematic of two cylinders in a side-by-side arrangement.

3.3.1. Two cylinders in a side-by-side arrangement. Considering a uniform flow past two cylinders in a side-by-side arrangement shown in Figure 15, there are two typical non-dimensional parameters to characterize this problem, i.e. the Reynolds number Re based on the diameter of cylinder D, and the spacing between the two cylinder surfaces $g^* = g/D$. A variety of flow patterns in the wake of the side-by-side cylinder array have been found in [46–49]. When the gap spacing is larger than one diameter of the cylinder, the flow is symmetrical with synchronous vortex streets. When the gap is gradually decreased, asymmetric unsteady regimes occur and the flow patterns change extensively, resulting in different vortex shedding frequencies for each cylinder. Further, when the gap is smaller than certain distances, the flow becomes steady state with deflect flow patterns.

DOI: 10.1002/fld

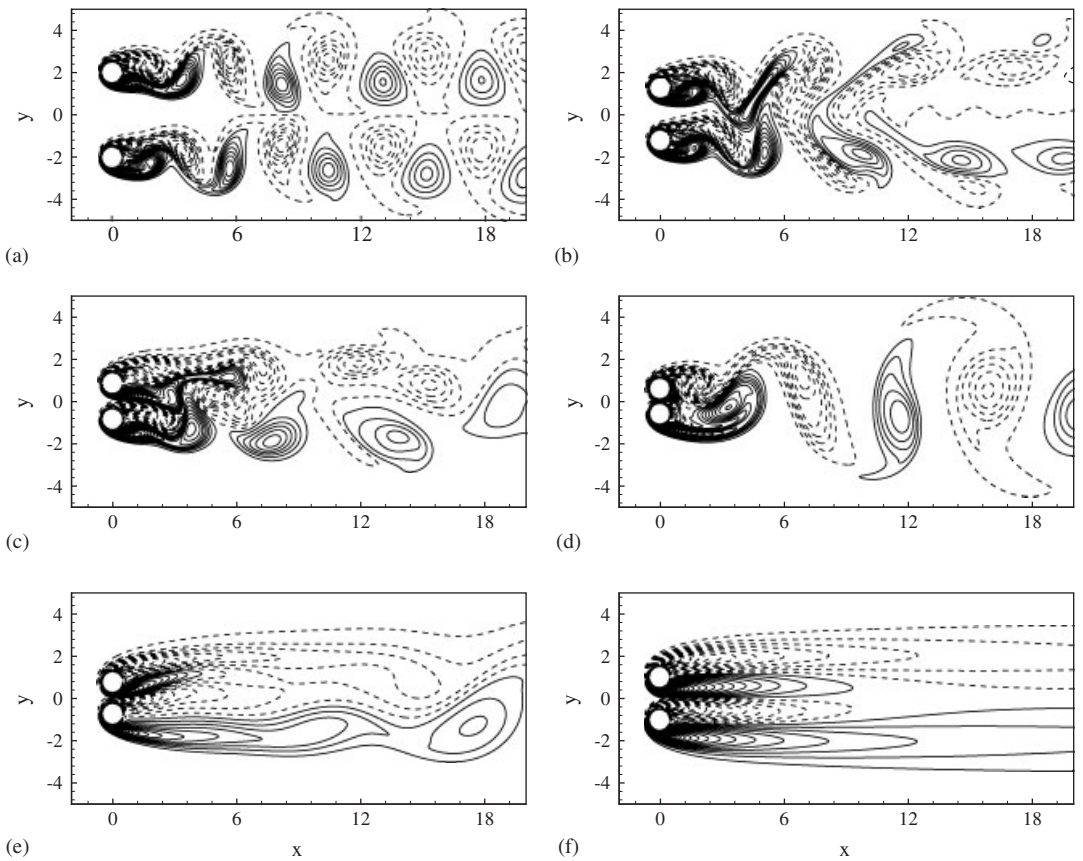

Figure 16. Instantaneous vorticity contours: (a) antiphase-synchronized pattern ($Re = 100$ and $g^* = 3$); (b) in-phase-synchronized pattern ($Re = 100$ and $g^* = 1.5$); (c) flip-flopping pattern ($Re = 100$ and $g^* = 0.7$); (d) single bluff-body pattern ($Re = 100$ and $g^* = 0.2$); (e) deflected pattern ($Re = 70$ and $g^* = 0.5$); and (f) steady pattern ($Re = 40$ and $g^* = 1$).

The influence of Re and g^* on the flow past two side-by-side circular cylinders at low Reynolds numbers has been investigated by Kang [46] using IBM. Six typical wake patterns, i.e. antiphase-synchronized, in-phase-synchronized, flip-flopping, deflected, single bluff body, and steady wake patterns, have been found. Here, we use this problem to examine the performance of the present method.

Here, as shown in Figure 15, the computational domain is $45D \times 30D$ in the x- and y-directions. Based on our calculations, six typical flow patterns in Figure 16 and force coefficient variations in Figure 17, consistent with the previous results [46, 48, 50], are reproduced.

Instantaneous vorticity contours for six wake patterns are shown in Figure 16(a)–(f). There are four corresponding distinct wake patterns for $Re = 100$, and $g^* = 3$, 1.5, 0.7 and 0.2. Figure 16(a)–(d) exhibits the antiphase-synchronized, in-phase synchronized, flip-flopping and single bluff-body state, respectively. When g^* is greater than D, the flow is symmetric and periodic, corresponding to the in-phase and antiphase patterns in Figure 16(a) and (b). In the flip-flopping

DOI: 10.1002/fld

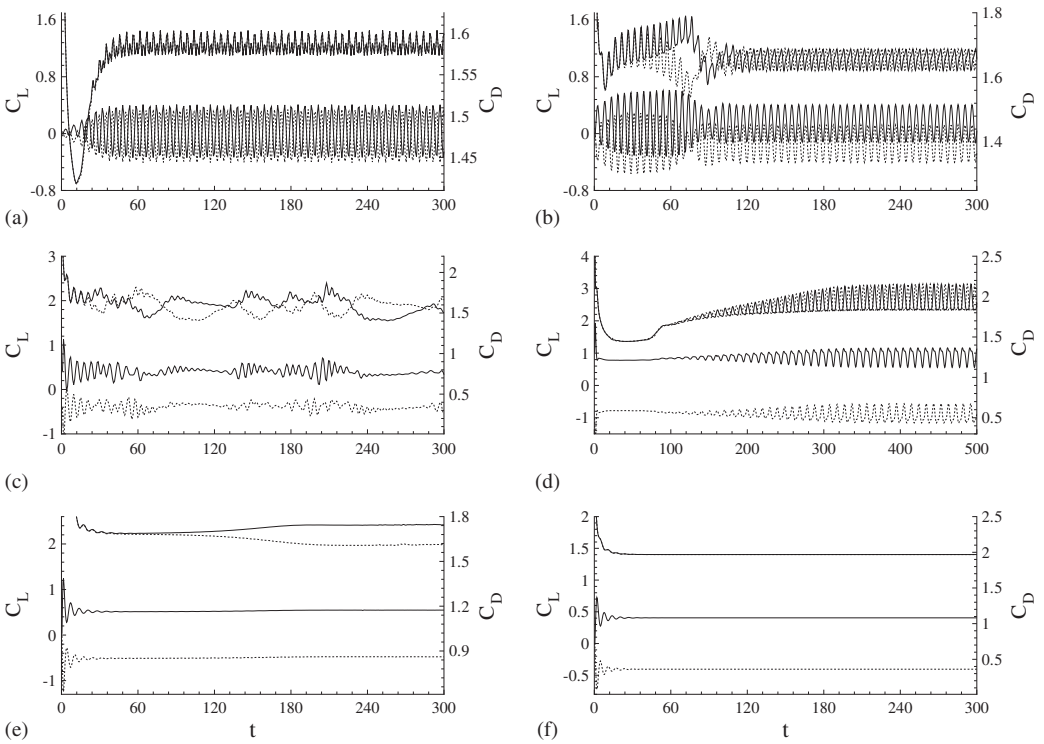

Figure 17. Time evolutions of the drag (two upper lines) and lift coefficients (two lower lines) for six flow patterns: (a) antiphase-synchronized pattern ($Re = 100$ and $g^* = 3$); (b) in-phase-synchronized pattern ($Re = 100$ and $g^* = 1.5$); (c) flip-flopping pattern ($Re = 100$ and $g^* = 0.7$); (d) single bluff-body pattern ($Re = 100$ and $g^* = 0.2$); (e) deflected pattern ($Re = 70$ and $g^* = 0.5$); and (f) steady pattern ($Re = 40$ and $g^* = 1$).

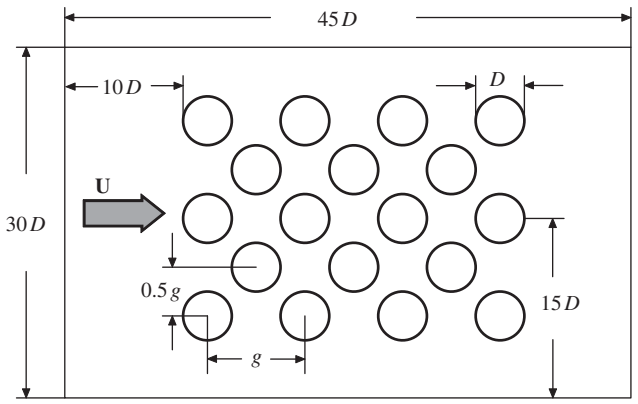

Figure 18. Schematic of flow past 18 cylinders in a staggered arrangement.

DOI: 10.1002/fld

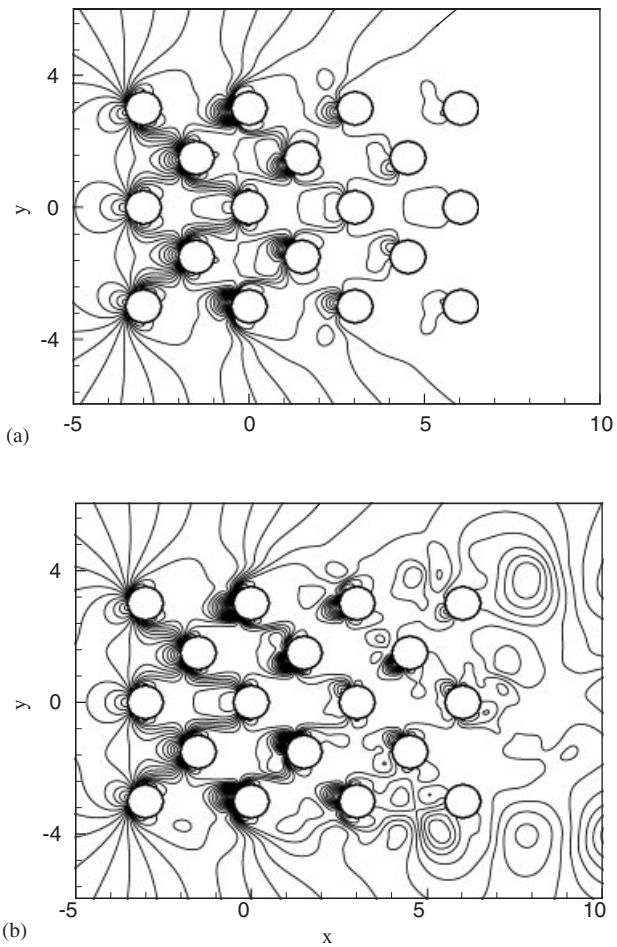

Figure 19. Instantaneous pressure contours of flow past an array of 18 staggered cylinders: (a) $Re = 100$ and (b) $Re = 200$.

pattern in Figure 16(c), the flow becomes unsteady and deflects to the higher-frequency cylinder side. The force coefficients in Figure 17(c) show that both the cylinders undergo irregular drag force. When both the cylinders are very close, e.g. $g^* = 0.2$, the flow within the gap becomes too weak to affect the global flow pattern. Therefore, the flow behaviour is similar to a single bluff-body pattern in Figure 16(d).

The effect of *Re* number on the flow structures is also investigated in Figure 16(e) and (f) for two typical flow patterns, namely deflected and steady wake patterns. Similar to the flip-flopping pattern in Figure 16(c), the deflection of the flow in Figure 16(e) is due to the higher drag force of one cylinder than the other. However, *Re* is so small that the viscous drag effectively counteracts the inertia momentum, and the flow turns to be steady again. When *Re* drops to 40, the flow becomes steady in Figure 16(f).

DOI: 10.1002/fld

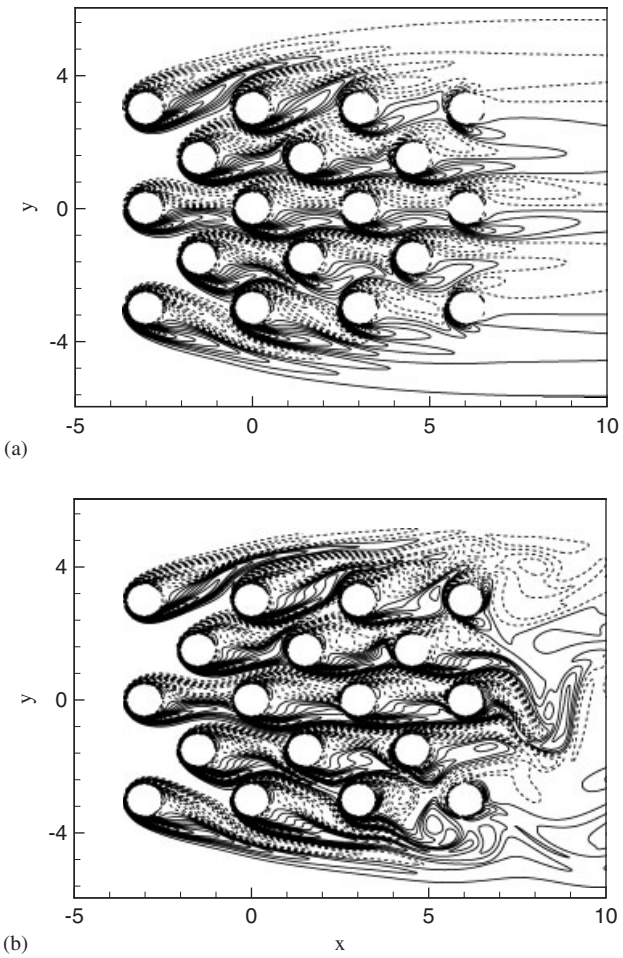

Figure 20. Instantaneous vorticity contours of flow past an array of 18 cylinders: (a) $Re = 100$ and (b) $Re = 200$.

3.3.2. Array of eighteen cylinders in a staggered arrangement. To further demonstrate the performance of the present method in more complex fluid–solid interactions, as shown in Figure 18, viscous flow past an array of 18 cylinders in a regular staggered arrangement is simulated. Similarly, two non-dimensional parameters $Re = UD/v$ and $g^* = g/D$ are used to describe the flow configuration, where g represents the distance between the centres of two neighbouring cylinders in either x- or y-direction.

Figures 19 and 20 show the pressure and vorticity contours at $Re = 100$ and 200. The flow is steady at $Re = 100$ and becomes unsteady with complex vortex shedding at $Re = 200$. It is well known that a periodic vortex shedding for uniform flow past a single circular cylinder occurs at $Re = 100$. However, steady flow pattern exists at the same Re for an array of 18 cylinders in Figures 19(a) and 20(a). Thus, unsteady vortex shedding is suppressed due to the interaction among the

DOI: 10.1002/fld

cylinders. To better understand the dynamics involved in this problem, further investigation should be required and is beyond the scope of this study. Basically, according to the computational test of this problem, the present method provides a possible approach to deal with the flow in multiple bluff bodies.

4. CONCLUDING REMARKS

An improved HCIB method based on the ghost point treatment has been proposed. The second-order Taylor series expansion is used to evaluate the values at the ghost points, and the IDW method to interpolate the values due to its properties of preserving the local extrema and smooth reconstruction. Compared with previous methods, the present approach eliminates numerical difficulties in the matrix inversion and maintains the accuracy of the algorithm. The IDW interpolation also provides a smooth and flexible boundary treatment to ensure the stability of the calculation.

To validate the present method, we have investigated some typical 2D and 3D flows, including viscous flows past a circular cylinder, a sphere, two cylinders in a side-by-side arrangement, and an array of 18 staggered cylinders. The grid resolution test indicates that overall second-order accuracy is achieved. These benchmark simulations confirm that the present method is efficient and reliable in dealing with fluid–solid flows.

ACKNOWLEDGEMENTS

This work was supported by the National Natural Science Foundation of China (Nos. 90405007 and 10332040), the Innovation Project of the Chinese Academy of Sciences, and the Program for Changjiang Scholars and Innovative Research Team in the University. The 2nd author (Y.-H.) acknowledged the support from the National Science Council (No. 95-2119-M-002-048). The authors gratefully thank the referees for valuable comments.

REFERENCES

1. Zienkiewicz OC. *The Finite Element Method in Engineering Science*. McGraw-Hill: London, 1971.
2. Hirt CW, Amsden AA, Cook JL. An arbitrary Lagrangian–Eulerian computing method for all flow speeds. *Journal of Computational Physics* 1974; **14**:227–253.
3. Tezduyar TE, Behr M, Liou J. A new strategy for finite element computation involving moving boundaries and interfaces—the deforming-spatial-domain/space–time procedure: I. The concept and the preliminary numerical tests. *Computer Methods in Applied Mechanics and Engineering* 1992; **94**:339–351.
4. Peskin CS. Flow patterns around heart valves: a numerical method. *Journal of Computational Physics* 1972; **10**:252–271.
5. Peskin CS. Numerical analysis of blood flow in the heart. *Journal of Computational Physics* 1977; **25**:220–252.
6. Zhu LD, Peskin CS. Simulation of a flapping flexible filament in a flowing soap film by the immersed boundary method. *Journal of Computational Physics* 2002; **179**:452–468.
7. Griffith BE, Peskin CS. On the order of accuracy of the immersed boundary method: higher order convergence rates for sufficiently smooth problems. *Journal of Computational Physics* 2005; **208**:75–105.
8. Lai MC, Peskin CS. An immersed boundary method with formal second-order accuracy and reduced numerical viscosity. *Journal of Computational Physics* 2000; **160**:705–719.
9. Goldstein D, Handler R, Sirovich L. Modeling a no-slip flow boundary with an external force field. *Journal of Computational Physics* 1993; **105**:354–366.
10. Ye T, Mittal R, Udaykumar HS, Shyy W. An accurate Cartesian grid method for viscous incompressible flows with complex immersed boundaries. *Journal of Computational Physics* 1999; **156**:209–240.

DOI: 10.1002/fld

11. Udaykumar HS, Mittal R, Rampunggoon P, Khanna A. A sharp interface Cartesian grid method for simulating flows with complex moving boundaries. *Journal of Computational Physics* 2001; **174**:345–380.
12. LeVeque RJ, Li Z. The immersed interface method for elliptic equations with discontinuous coefficients and singular sources. *SIAM Journal on Numerical Analysis* 1994; **31**:1019–1044.
13. Lee L, LeVeque RJ. An immersed interface method for incompressible Navier–Stokes equations. *SIAM Journal on Scientific Computing* 2003; **25**:832–856.
14. Xu S, Wang ZJ. Systematic derivation of jump conditions for the immersed interface method in three-dimensional flow simulation. *SIAM Journal on Scientific Computing* 2006; **27**:1948–1980.
15. Xu S, Wang ZJ. An immersed interface method for simulating the interaction of a fluid with moving boundaries. *Journal of Computational Physics* 2006; **216**:454–493.
16. Fadlun EA, Verzicco R, Orlandi P, Mohd-Yusof J. Combined immersed-boundary finite-difference methods for three-dimensional complex flow simulations. *Journal of Computational Physics* 2000; **161**:35–60.
17. Mohd-Yusof J. Combined immersed-boundary/B-spline methods for simulations of flow in complex geometries. *Annual Research Briefs*, Center for Turbulence Research, NASA Ames and Stanford University, 1997; 317–327.
18. Gilmanov A, Sotiropoulos F. A hybrid Cartesian/immersed boundary method for simulating flows with 3D, geometrically complex, moving bodies. *Journal of Computational Physics* 2005; **207**:457–492.
19. Tseng YH, Ferziger JH. A ghost-cell immersed boundary method for flow in complex geometry. *Journal of Computational Physics* 2003; **192**:593–623.
20. Tseng YH, Meneveau C, Parlange MB. Modeling flow around bluff bodies and predicting urban dispersion using large eddy simulation. *Environmental Science and Technology* 2006; **40**:2653–2662.
21. Yang JM, Balaras E. An embedded-boundary formulation for large-eddy simulation of turbulent flows interacting with moving boundaries. *Journal of Computational Physics* 2006; **215**:12–40.
22. Majumdar S, Iaccarino G, Durbin P. RANS solvers with adaptive structured boundary non-conforming grids. *Annual Research Briefs*, Center for Turbulence Research, NASA Ames and Stanford University, 2001; 353–366.
23. Fedkiw RP, Aslam T, Merriman B, Osher S. A non-oscillatory Eulerian approach to interfaces in multimaterial flows (the ghost fluid method). *Journal of Computational Physics* 1999; **152**:457–492.
24. Ferziger JH, Perić M. *Computational Methods for Fluid Dynamics* (3rd edn). Springer: Berlin, 2001.
25. Franke R. Scattered data interpolation: tests of some methods. *Mathematics of Computation* 1982; **38**:181–200.
26. Watson DF, Philip GM. A refinement of inverse distance weighted interpolation. *Geo-Processing* 1985; **2**:315–327.
27. Kim J, Moin P. Application of a fractional-step method to incompressible Navier–Stokes equations. *Journal of Computational Physics* 1985; **59**:308–323.
28. Rai MM, Moin P. Direct simulations of turbulent flow using finite-difference schemes. *Journal of Computational Physics* 1991; **96**:15–53.
29. Verzicco R, Orlandi P. A finite-difference scheme for three-dimensional incompressible flows in cylindrical coordinates. *Journal of Computational Physics* 1996; **123**:402–414.
30. Harlow FH, Welsh JE. Numerical calculation of time-dependent viscous incompressible flow of fluid with free surfaces. *Physics of Fluids* 1965; **8**:2182–2189.
31. Mittal R, Iaccarino G. Immersed boundary methods. *Annual Review of Fluid Mechanics* 2005; **37**:239–261.
32. Iaccarino G, Verzicco R. Immersed boundary technique for turbulent flow simulations. *Applied Mechanics Reviews* 2003; **56**:331–347.
33. Shu C, Wu YL. Adaptive mesh refinement-enhanced local DFD method and its application to solve Navier–Stokes equations. *International Journal for Numerical Methods in Fluids* 2006; **51**:897–912.
34. Sonneveld P. CGS, A fast Lanczos-type solver for nonsymmetric linear systems. *SIAM Journal on Scientific and Statistical Computing* 1989; **10**:36–52.
35. Van der Vorst HA. Bi-CGSTAB: a fast, smoothly converging variant of Bi-CG for the solution of nonsymmetric linear systems. *SIAM Journal on Scientific and Statistical Computing* 1992; **13**:631–644.
36. Stone HL. Iterative solution of implicit approximations of multidimensional partial differential equations. *SIAM Journal on Numerical Analysis* 1968; **5**:530–558.
37. Park J, Kwon K, Choi H. Numerical solutions of flow past a circular cylinder at Reynolds numbers up to 160. *KSME International Journal* 1998; **12**:1200–1205.
38. Lima e Silva ALF, Silveira-Neto A, Damasceno JJR. Numerical simulation of two-dimensional flows over a circular cylinder using the immersed boundary method. *Journal of Computational Physics* 2003; **189**:351–370.
39. Tritton DJ. Experiments on the flow past a circular cylinder at low Reynolds number. *Journal of Fluid Mechanics* 1959; **6**:547–567.
40. Williamson CHK. Vortex dynamics in the cylinder wake. *Annual Review of Fluid Mechanics* 1996; **28**:477–539.

DOI: 10.1002/fld

41. Kim D, Choi H. Immersed boundary method for flow around an arbitrarily moving body. *Journal of Computational Physics* 2006; **212**:662–680.
42. Taneda S. Experimental investigation of the wake behind a sphere at low Reynolds numbers. *Journal of the Physical Society of Japan* 1956; **11**:1104–1108.
43. Johnson TA, Patel VC. Flow past a sphere up to a Reynolds number of 300. *Journal of Fluid Mechanics* 1999; **378**:19–70.
44. Constantinescu GS, Squires KD. LES and DES investigations of turbulent flow over a sphere. *AIAA paper-2000-0540*.
45. Jeong J, Hussain F. On the identification of a vortex. *Journal of Fluid Mechanics* 1995; **285**:69–94.
46. Kang S. Characteristics of flow over two circular cylinders in a side-by-side arrangement at low Reynolds numbers. *Physics of Fluids* 2003; **15**:2486–2498.
47. Bearman PW, Wadcock AJ. The interaction between a pair of circular cylinders normal to a stream. *Journal of Fluid Mechanics* 1973; **61**:499–511.
48. Williamson CHK. Evolution of a single wake behind a pair of bluff bodies. *Journal of Fluid Mechanics* 1985; **159**:1–18.
49. Zhou Y, Wang ZJ, So RMC, Xu SJ, Jin W. Free vibrations of two side-by-side cylinders in a cross flow. *Journal of Fluid Mechanics* 2001; **443**:197–229.
50. Zdravkovich MM. Review of flow interference between two circular cylinders in various arrangements. *Journal of Fluids Engineering* (ASME) 1977; **99**:618–633.

DOI: 10.1002/fld